EFDA–JET–CP(14)01/16

M. Lehnen, K. Aleynikova, P.B. Aleynikov, D.J. Campbell, P. Drewelow, N.W. Eidietis, Yu. Gasparyan, R.S. Granetz, Y. Gribov, N. Hartmann, E.M. Hollmann, V.A. Izzo, S. Jachmich, S.-H. Kim, M. Kocan, H.R. Koslowski, D. Kovalenko, U. Kruezi, A. Loarte, S. Maruyama, G.F. Matthews, P.B. Parks, G. Pautasso, R.A. Pitts, C. Reux, V. Riccardo, R. Roccella, J.A. Snipes, A.J. Thornton, P.C. de Vries and JET EFDA contributors

Disruptions in ITER and Strategies for their Control and Mitigation

Disruptions in ITER and Strategies for their Control and Mitigation

M. Lehnen[1], K. Aleynikova[1], P.B. Aleynikov[1], D. J. Campbell[1], P. Drewelow[2], N.W. Eidietis[3], Yu. Gasparyan[4], R.S. Granetz[5], Y. Gribov[1], N. Hartmann[6], E.M. Hollmann[7], V.A. Izzo[1], S. Jachmich[8], S.-H. Kim[1], M. Kočan[1], H.R. Koslowski[6], D. Kovalenko[9], U. Kruezi[10], A. Loarte[1], S. Maruyama[1], G.F. Matthews[10], P.B. Parks[3], G. Pautasso[11], R.A. Pitts[1], C. Reux[12], V. Riccardo[10], R. Roccella[1], J.A. Snipes[1], A.J. Thornton[10], P.C. de Vries[1] and JET EFDA contributors*

JET-EFDA, Culham Science Centre, OX14 3DB, Abingdon, UK

[1]ITER Organization, Route de Vinon sur Verdon, 13115 St Paul Lez Durance, France
[2]Max-Planck-Institut für Plasmaphysik, Greifswald branch, EURATOM Ass., D-17491 Greifswald, Germany
[3]General Atomics, P.O. Box 85608, San Diego, California 92186-5608,USA
[4]National Research Nuclear University MEPhI (Moscow Engineering Physics Institute), Moscow, Kashirskoe sh. 31, 115409, Russia
[5]MIT Plasma Science and Fusion Center, Cambridge, MA 02139, USA
[6]Forschungszentrum Jülich GmbH, Institute of Energy and Climate Research—Plasma Physics, Association EURATOM-FZJ, Trilateral Euregio Cluster, 52425 Jülich, Germany
[7]University of California-San Diego, La Jolla, California 92093, USA
[8]Laboratory for Plasma Physics, ERM/KMS, Association EURATOM – Belgian State, B-1000 Brussels, Belgium
[9]SRC RF TRINITI, ul. Pushkovykh, vladenie 12, Troitsk, Moscow Region, 142190, Russia
[10]EURATOM-CCFE Fusion Association, Culham Science Centre, OX14 3DB, Abingdon, OXON, UK
[11]Max-Planck-Institut für Plasmaphysik, EURATOM Association, D-85748 Garching, Germany
[12]CEA, IRFM, F-13108 Saint-Paul-lez-Durance, France
** See annex of F. Romanelli et al, "Overview of JET Results", (24th IAEA Fusion Energy Conference, San Diego, USA (2012)).*

Preprint of Paper to be submitted for publication in Proceedings of the
21st International Conference on Plasma Surface Interactions, Kanazawa, Japan
26th May 2014 - 30th May 2014

ABSTRACT

The thermal and electromagnetic loads related to disruptions in ITER are substantial and require careful design of tokamak components to ensure they reach the projected lifetime and to ensure that safety relevant components fulfil their function for the worst foreseen scenarios. The disruption load specifications are the basis for the design process of components like the full-W divertor, the blanket modules and the vacuum vessel and will set the boundary conditions for ITER operations. This paper will give a brief overview on the disruption loads and mitigation strategies for ITER and will discuss the physics basis which is continuously refined through the current disruption R&D programs.

1. INTRODUCTION

The energy stored during a burning plasma pulse in ITER will significantly exceed that in present devices. Rapid release of this energy during a disruption has the potential to cause surface melting of plasma-facing components (PFC) and will cause high electromagnetic loads close to the design limits. Hence, successful exploitation of ITER will depend on establishing reliable and effective strategies to predict and avoid disruptions and - as a final line of defence - to mitigate disruptions. Deriving an improved characterisation of disruption loads and developing robust means of their mitigation which can be extrapolated reliably to the ITER scale are two of the major outstanding challenges in current tokamak R&D for ITER.

The projected thermal loads on the full-W divertor and the Be first wall (FW) in ITER during unmitigated major disruptions and vertical displacement events (VDE) can, at high plasma energies, exceed the surface melting threshold by significant factors [1], [2]. High energy loads are conservatively taken to estimate the lifetime of components, but especially for planning the early phase of ITER operation it is also essential to know the threshold energies at which loads start causing melt damage. Initial calculations show that heat loads arising during the current quench that follows the loss of thermal energy can also cause surface melting of the FW. Formation of runaway electrons is a particular issue as these electrons will deposit their energy - which can be a significant fraction of the stored magnetic energy – in localised regions of the bulk material, and could potentially penetrate cooling channels, causing water leaks. However, one has to be aware that all these estimates and calculations are based on empirical findings, providing typical timescales and spatial distributions, and a better understanding of the underlying physics is part of the present disruption research (see Section 2.1).

Electromagnetic (EM) forces arise from eddy currents during the fast decay of plasma current and from halo currents during fast vertical displacements of the plasma column. These forces act on blanket modules, magnets and the vacuum vessel. The last of these is the first confinement barrier and must be designed to withstand the highest predicted EM loads. The EM loads, their categorisation, and the impact of recent results with full metal walls in JET are discussed in Section 2.2.

Disruption avoidance relies on the plasma control system keeping the plasma within the pre-

programmed operation window. It can be expected that pre-pulse stability analysis will decrease the risk of disruptions. Nevertheless, disruptions will not be avoidable with 100% reliability. The plasma control system should be able to forecast instabilities and predict disruptions and trigger an appropriate control response. Should it be impossible to recover a stable situation, the disruption mitigation system (DMS) will have to be activated, reacting appropriately to the specific situation (see Section 3).

The DMS for ITER is presently in the design phase, with two main candidates: massive gas injection (MGI) and shattered pellet injection (SPI) (Section 3.1). A decision on the final design is scheduled to be taken in 2017. The physics basis for disruption control is, to a large extent, being established within dedicated ITPA (International Tokamak Physics Activity) experiments and accompanying modelling efforts. The challenging task for the ITER DMS is to ensure simultaneously: a) the reduction of heat loads to limit melting of PFCs to a tolerable degree (Section 3.2), b) the reduction of halo currents and their toroidal peaking to reduce the occurrence of severe load events (Section 3.3) and c) mitigation or suppression of runaway electrons (Section 3.4), and to satisfy all of these aims while staying within a narrow operating window with respect to current quench times and injected quantity of material.

2. LOADS ASSOCIATED WITH DISRUPTIONS IN ITER

2.1 THERMAL LOADS

Thermal loads in ITER stem from thermal stored energy that is lost during the thermal quench (TQ) phase of the disruption, from magnetic energy that is conducted to plasma facing components during the current quench and from the impact of high energy runaway electrons. Especially in the early operational phase these loads have to be carefully monitored to identify load limits and mitigation needs. The heat loads during major disruptions (MDs) on the full-W divertor have been assessed in [2] with no-damage threshold energies found below around 25 MJ. The impact of high energy VDEs on the lifetime of the beryllium first wall (FW) panels has been analysed in [1]. Here, a first analysis of FW melt damage during MDs and from conductive losses of the magnetic energy is presented.

To assess FW melt damage, first the heat flux distribution is determined by mapping outer mid-plane profiles to the FW panels using the field line tracing code PFCFLUX [3]. Melted and evaporated masses are then estimated from the code RACLETTE [4]. The energy flux during the thermal quench of a major disruption to the first wall has been varied using different stored thermal energies and different e-folding lengths to cover the expected range of footprint broadening in ITER [5]. The energy is deposited, rising linearly in 1.5ms followed by a 3ms decay. This is in accordance with the ITER specification for MD heat loads (VDE heat loads are assumed to be a factor of 2 faster). Depending on the broadening, the energy fraction to the first wall increases from 5% (λ_E = 30mm) to 23% (λ_E = 90mm). The main part of the energy is expected to load the divertor target plates. On the FW, it is especially the inboard side and the second separatrix area that receives the main load. From Figure 1b, a threshold for surface damage at energies of about 50 MJ can be identified.

Unmitigated major disruptions (as well as VDEs [1]) at high stored energies can cause masses of the order of kilograms to be melted. How much of this material will be mobilised and eventually converted into dust depends on whether Rayleigh-Taylor instabilities driven by eddy currents can develop during these fast transients [6].

Measuring the heat flux and the energy distribution on the FW and the divertor during disruptions is especially challenging because of the short timescales involved. Moreover, as the example from DIII-D given in Figure 2a shows, the measured heat flux profile (red line) can be a combination of conducted heat and heat caused by intense plasma radiation (blue line). In addition, background radiation in the infra-red range (cyan line) can obstruct the measurement. Thus, quantifying the footprint broadening, which is expected to depend on the specific development of the MHD during the TQ (heat flux profiles for different disruption types can be found for example in [7]), bears high uncertainties. Figure 2b shows an example of the heat flux evolution on a spherical limiter in TEXTOR during the thermal quench of a low q disruption. The broadening is quite small – about a factor of 2 – and only observed on one side of the limiter. Additionally, local peaks on the profile indicate that the heat deposition is driven by macroscopic MHD. A third example from ASDEX Upgrade for a density limit disruption shows a very broad distribution of the energy on the FW and the divertor. Remarkable here is that, because of the secondary separatrix in this upper single null configuration, a non-negligible heat flux is found in the lower divertor because of the highly enhanced radial transport. Also, in ITER, this is the reason for substantial heat going to the panels of blanket module (BM) 8 and 9 (indicated by the blue dots in Figure 1a). A full balance, including the energy being conducted to the FW/divertor and that being radiated, has not been achieved in the experiments so far. DIII-D data shows a high fraction of thermal energy arriving in the divertor of about 50-100% for beta limit disruptions and VDEs and less for radiative limits [8]. In contrast, at JET, only a small fraction of the order of 10% of the stored energy is detected in the divertor, however, the IR camera view is restricted to the outer divertor only [9].

Insufficient levels of radiation during the current quench can cause magnetic energy to be converted into heat flux to first wall panels and/or divertor target plates. This has caused melting of PFCs in JET with the ITER-like wall as reported in [10, 11, 12]. Here, besides the amount of deposited energy, the timescale of the heat deposition is important as can be seen from figure 15 in [12]. Indeed, melting is expected to have occurred during fast vertical displacements with low radiation fraction. Conductive loss of magnetic energy is not only restricted to JET with its full metal plasma facing components (PFCs), but was also observed at other devices during unmitigated disruptions. At ASDEX Upgrade with a carbon wall, 30% of the magnetic energy was detected in the divertor [13] and even higher fractions of more than 70% are commonly measured in MAST [14]. Similar to JET findings, C-Mod also reports slow current quenches with high temperatures and low radiation [15].

A first assessment of CQ heat loads during a VDE in ITER is shown in Figure 1c. Because of the fractional poloidal shape of the ITER FW, the plasma touching point of the FW will not move

continuously but rather reside for a certain time at one position and then jump to the next panel. In the example shown, the touching point resides for about 70 ms on BM 10 in the first phase of the CQ in which about 30% of the magnetic energy is lost. The remaining energy is deposited on BMs 9 and 8. The VDE has been simulated with the code DINA [16] with a prescribed current decay time of about 200 ms. In reality the current decay will be determined by the power balance between Ohmic heating, transport driven loss, and radiation. The analysis of the FW damage on BM 10 shows that, above a critical plasma current, material melting cannot be excluded. A similar threshold can be expected for MDs, which also will be vertically displaced during the CQ, however touching the first wall at already reduced plasma current.

Runaway electrons (RE) formed during the current quench represent a high risk for the lifetime of the affected components like the FW panels, divertor baffles, or the dome. This is because of the distinct features of the runaway impact: small impact area, fast timescales and deep penetration into the bulk of the component. It is expected that currents of up to 10 MA could form in ITER carrying a kinetic energy of about 20 MJ. However, still a high fraction of magnetic energy remains in the poloidal field of this current. Depending on the timescale of the runaway loss, a significant fraction of this magnetic energy can be converted into kinetic energy as shown in Figure 3a [17, 18].

The wetted area and the deposition duration depend strongly on the RE loss mechanism. Vertical or radial displacement of the RE beam can lead to "scraping-off" of REs. On the other hand a fast loss of the entire RE beam on a sub-millisecond timescale is possible. Although it is thought that MHD instabilities related to q = 2 are responsible for this fast loss, this has not been confirmed experimentally yet [19]. Both phenomena have been observed in the experiments. The impact area during "scraping-off" has been measured at TEXTOR using a spherical test limiter (Figure 3b). During the impact of about 3 kJ of RE energy (according to thermocouple data) over about 10ms a temperature rise to the sublimation point was measured. The radial extent of the impact area can be attributed to the gyro-motion of the runaways with a Larmor radius of about 2mm (see Figure 3b). This is consistent with estimates of the pitch angle ranging from 0.08 [20] to 0.2 [19]. The deviation from this surface load estimate on the ion side can be attributed to volume deposition of the RE energy. For comparison the normal SOL heat flux distribution with thermal flow velocities is shown (blue dashed line). The poloidal extent of the RE impact area can be estimated using the simplifying assumption of a poloidally flat FW structure:

$$\theta = 2\sqrt{(r_{RE} + r_L)^2 - r_{RE}^2}.$$

A runaway beam radius of $r_{RE} = 0.5$m in JET yields with the pitch angles given above a poloidal extent ofmm. These numbers are consistent with previous JET observations during fast loss events [21] as well as more recent experiments with Ar MGI [22]. Also at JT-60U, a small poloidal extent of the RE heat flux of about 200 mm has been observed during fast RE loss events of less than 0.25 ms duration [23]. The above consideration assumes a RE beam in limiter configuration. A

special situation can occur when an X-point is present during the RE phase of the disruption. This can lead to RE impact in more remote areas of the first wall as has been observed at Tore Supra [24].

2.2 ELECTRO-MAGNETIC LOADS

Relevant electro-magnetic (EM) loads are arising during the current quench phase of the disruption when halo currents are generated during vertical displacements and the fast decay of plasma current induces eddy currents in the FW structure. Figure 4a shows a sketch of a downward VDE in ITER. The halo current flows in an outer shell around the plasma and enters the FW structure around the plasma contact point. Depending on inductances and resistivities it will follow a path through the BMs, divertor, and vacuum vessel (VV) resulting in poloidal currents that –together with the toroidal magnetic field - give rise to forces. Whereas halo currents are the main contributor to the forces on the VV, eddy currents are the more critical currents for the BMs where they lead to poloidal forces on the structural elements fixing the BMs [25]. The toroidal distribution of the halo currents in the structure is not necessarily symmetric and the degree of asymmetry is quantified in the toroidal peaking factor (TPF), which is the maximum poloidal halo current normalised to the toroidal average. These asymmetries give for example rise to sideways and/or tilting forces on the VV. Of special concern is rotation during asymmetric events as observed at JET [26] or NSTX [27] as this could potentially cause dynamic amplification of loads. This issue is currently addressed by 3D MHD modelling [28] and by a dedicated effort within ITPA.

The design process of the ITER components requires quantification and categorisation of EM loads. Categorisation of events starts from normal operation and likely events with well acceptable loads (cat. I) and ends at extremely unlikely loading conditions (cat. IV). During the ITER lifetime 2600 MDs of cat. I, 400 MDs of cat. II and 300 VDEs of cat. II are projected. Cat. III events are allowed to happen only once or twice during the ITER lifetime and will result in substantial loss of operational time as an extensive inspection of safety relevant components has to be performed. The requirements for these safety relevant components – like for example the VV – are very strict and the design has to ensure their safety function even after a cat. IV event. The load definition for cat I MD is a linear current decay time equal to or more than 50ms and a maximum TPF x I_H/I_P of 0.15 (I_H = halo current, I_P = plasma current). MDs of cat. II events are limited to 36 ms with the same constraint for the halo current. VDEs are generating much higher halo currents and the worst case VDEs of cat. III have long current quench times and TPF x I_H/I_P = 0.75 with maximum halo current of 8.2 MA for downward VDEs. Cat. II VDEs have halo current limits reduced to 56% of those for cat. III. Upward VDEs are expected to have a smaller quadrupolar field in ITER and therefore the load limit is reduced by 20% for these VDEs.

The load estimates have been refined in the course of the design process of the VV and the BMs compared to previous assessments [25]. Figure 4b shows the forces resulting from eddy and halo currents on BM 1 that will bear the most severe load of all BMs during a downward VDE with a fast CQ. It can be seen that these loads are due to eddy currents because of the short current decay

time of 36 ms. In contrast, a VDE with a slow CQ will result in negligible eddy currents and a maximum halo current of 8.2MA, still well below the force limits (blue data point). The VV loads are dominated by halo currents and the load limits are compared to data from the ITPA disruption database [29, 30] in Figure 4c. Whether the actual halo currents will be as high as seen in many devices is not obvious, especially because of the much smaller vertical growth times predicted for ITER. However, because of the findings with the JET ITER-like wall [11, 12], it may be expected with the full-W divertor of ITER that long current quenches will be likely and this could increase the probability for cat. III events. It will be an important task of the ITER Disruption Mitigation System (DMS) to accelerate the CQ to keep the loads from halo currents within the cat II boundary.

3. LOAD MITIGATION SCHEMES

ITER load mitigation comprises highly reliable disruption prediction, active schemes for disruption avoidance and a disruption mitigation system that reduces thermal and electromagnetic loads. This section summarises the mitigation needs, the available techniques and discusses the issues related to load mitigation.

Disruption mitigation in ITER is essential for the avoidance of melt damage in the full W-divertor and the Be first wall and especially important for the reduction of EM loads in order to prevent cat. III events as outlined in the previous section. The operational space in ITER in terms of thermal energy and plasma current is shown in Figure 5. The green area indicates the parameters for which unmitigated disruptions are expected to stay within the no-damage limit, which is mainly given by the TQ heat flux to the inner divertor and the CQ heat flux to the first wall. Note that a threshold for REs is not given here, because of the large uncertainties in the energy they could potentially deposit on PFCs. Above about $I_p = 8.4$MA, unmitigated disruptions are more likely to be cat III, due to high halo current levels because of the expected slow current decay. Considering the number of pulses planned for high current, high field operation, a very high reliability to reduce the CQ duration, is required from the DMS. As the operational range is expanded, the loads will increase (indicated by the maximum expected thermal energies [31]), posing higher requirements for mitigation efficiency (i.e. the radiative fraction). Note, that Ohmic, full current disruptions can already cause melt damage.

3.1 DISRUPTION MITIGATION SYSTEM

The ITER DMS is supposed to inject impurities to increase radiation and by this reduce thermal loads and accelerate the CQ. Two injection schemes are presently under consideration, Massive Gas Injection (MGI) and Shattered Pellet Injection (SPI). A broad experimental database exists for MGI [7, 15, 32, 33, 34, 14] and we will focus mainly on these results in the following. Cryogenic pellet injection has proven in the past to be capable of reducing loads [35, 36, 37, 38], but it is not considered an option for ITER because of the high risk of generating RE. SPI results in better assimilation thereby avoiding RE formation [39]. This technique has been successfully tested at DIII-D with D_2 pellets [40] and further experiments with high-Z impurities are planned.

In ITER, three upper port plugs are allocated for the installation of DMS components as well as one equatorial port. All port plugs will be utilised for thermal and electromagnetic load mitigation, whereas the equatorial port will contain, in addition, a system dedicated to runaway mitigation/ suppression. An example of the integration of SPI in one of the upper port plugs is given in Figure 6. The amount of injected impurities will be limited to 8kPam^3 for thermal load mitigation (TLM), while for RE suppression the limits will be 100kPam^3 for neon and argon, 50 kPam^3 for deuterium and 40kPam^3 for helium [41]. The limits for the noble gases avoid spontaneous regeneration of the torus cryo-pumps and related downtimes. The maximum amount of deuterium is determined by the deflagration limit. Each system can be activated separately with adjustable time delays that will be determined in real-time by the Plasma Control System (PCS) to provide the most flexible answer to the mitigation requirements.

An important design parameter for the DMS is the time delay between activation and initiation of the mitigated TQ, which is sometimes referred to as reaction time. For SPI this includes the time of flight from injector to plasma and the time needed for assimilation and MHD growth. For MGI the process involves the gas flow in the delivery tube and the penetration of the cold front into the plasma, the latter being referred to as cooling duration in the following. It has been shown at various tokamaks that the TQ is initiated when the cold front reaches the surface [42, 7, 32, 33, 43]. Note, that the DMS will be activated when the plasma performance is already degraded and this can reduce the cooling duration significantly [44]. Figure 7a shows the normalised cooling duration for various tokamaks as function of the radiated energy per injected atom. From this database, one finds an empirical lower limit for the cooling duration in ITER of about 6 ms assuming that 8 kPam^3 of impurities are injected at the time of the thermal quench. However, an important question is if the flow rate can be high enough to inject the required gas quantity on this timescale. Figure 7b shows the injected quantity and the total delay to the TQ including time of flight and assuming that the TQ onset happens when the thermal energy outside has been radiated (about 20% of the total energy in ITER). The calculation is based on a simplified flow model without depletion of the reservoir [34] and assumes a fixed radiation efficiency . It becomes obvious that high injection efficiencies require large valve orifices and/or short distances from the valve to the plasma.

Thermal load mitigation

The ITER DMS aims to establish radiation fractions at high thermal energies of . However, during first operation, thermal energies will be much lower compared to the target DT plasma with and, therefore, mitigation requirements will be less demanding (c.f. Figure 5). This phase will be used to optimise mitigation in preparation for high performance operation. Although simulations with ASTRA [45] and NIMROD [46] show that high radiation fraction can be achieved with MGI, still, large scatter remains in the experimental data (Figure 10). Measuring the radiation fraction during the TQ – as done in DIII-D – requires fast time resolution and accurate separation between the TQ and the CQ. Alternatively, as done for the other devices, the radiation fraction can be determined for the entire disruption. However, this requires an estimate of the fraction of magnetic energy being

dissipated in the surrounding structure during the current quench. This has been done for JET and could be the reason for lower found in ASDEX Upgrade and Alcator C-Mod. Nevertheless, JET data shows still a large variation and, moreover, at high thermal energies saturates at about 80% despite further increase in injected argon.

Besides the above mentioned uncertainties in determining the radiation fraction, toroidal asymmetries can affect the accuracy of as well. Moreover, radiation asymmetries could cause local heat loads that exceed the melting limit of beryllium of the ITER FW or the stainless steel in front of the diagnostic ports [47]. Before the onset of the TQ, radiation asymmetries can be reduced by injecting simultaneously at different toroidal locations as shown in Alcator C-Mod [48] and in simulations [49]. However, during the TQ the radiation distribution is expected to be determined by macroscopic MHD [46]. NIMROD calculations for DIII-D show that poloidal and toroidal asymmetries are driven mainly by the dominant n=1 mode during the TQ (Figure 8). This results in a toroidal peaking factor of 2.1, despite the toroidally uniform impurity injection in this particular simulation. Experiments show relatively small toroidal radiation peaking during the TQ well below 2 for DIII-D [50] and ASDEX Upgrade [44] and slightly higher for Alcator C-Mod, depending on the injection timing of the valves [51]. The impact of MHD modes on the radiation distribution has been shown in experiments using external n = 1 fields to lock the TQ modes. A clear correlation between radiation distribution and the field phase has been found at DIII-D and JET but with still low toroidal peaking (Figure 9). Also at ASDEX Upgrade, the radiation peaking is not significantly affected by the existence of locked modes at the start of the TQ [44]. Although the experimentally observed low toroidal peaking is promising in view of radiation heat loads during mitigation, a definitive answer can only be given with more information on how far the toroidal and poloidal distribution of the injectors or the MHD rotation and dominant mode number affects radiation peaking.

3.3 ELECTRO-MAGNETIC LOAD MITIGATION

The aim of EM load mitigation is to reduce halo currents in order to prevent category III events (see section 2.2) whilst keeping eddy current loads acceptable. At full plasma current of 15 MA, these requirements result in an operational window for the CQ decay time of 50-150 ms. However, at lower current during the initial operation of ITER, shorter CQs are also within the load limits. A conservative assumption is a linear dependence of these limits on plasma current. In Figure 11, these limits are compared to normalised linear current decay times found at JET with an ITER-like wall. Because of the increase in Ohmic heating, CQ times become longer for higher plasma currents at constant impurity level. This is illustrated by the black line resulting from simplified power balance calculations [12]. CQ times are systematically shorter in a carbon environment compared to metallic walls because of the contribution of carbon to the total radiated power. Thus, the choice of a full-W divertor for ITER helps keep a sufficient margin to the load limits. Moreover, the lack of carbon radiation increases the controllability of the CQ by impurity injection.

The fraction of poloidal halo current being generated during the CQ depends on the competition between current decay and vertical displacement [52]. For sufficiently fast CQs the safety factor stays high and poloidal halo currents are only a fraction of the toroidal currents. As shown in Figure 12, DINA simulations as well as experimental data show a significant reduction of poloidal halo currents with fast CQs. Usually, together with the reduction in halo current, there is also a reduction of the TPF with MGI. This is not the case for MAST, for which the TPF increases with decreasing . The origin of this deviation remains to be identified. In view of the extremely demanding requirements on reliability to prevent cat. III events, it is important to note that also late injection after the TQ into a slowly developing CQ can still accelerate the current decay sufficiently and prevent high halo currents [12]. However, very late injection during a VDE can result in reduced mitigation efficiency [53, 54].

3.4 RUNAWAY SUPPRESSION

Since the installation of the ITER-like wall at JET, runaway formation has not been observed, which is likely to be due to the small electric fields during the slow CQs [22]. Although this result appears promising for ITER, it has to be kept in mind that impurity injection is foreseen for thermal load mitigation, which has an impact on the CQ rate and on the temperature and density evolution and, therefore, also on the potential development of REs. The mitigation of disruption heat loads and forces, must avoid generation of hot tail or Dreicer induced REs, thus removing the seed for avalanche amplification. Note that the amplification factor in ITER is orders of magnitude higher than in present devices. During the activated phase of ITER, sources independent of the evolution of the disruption, i.e. tritium decay and Compton-scattering, will impose a requirement for suppression of the avalanche by the DMS. A suitable scheme for the active suppression or mitigation of runaway electrons has not yet been confirmed. Various options have been addressed in experiments and are summarised in this section.

RE suppression by densification aims to reach the critical electron density above which any RE generation is prevented. For a CQ time of 50 ms, the toroidal electric field is of the order of 30 V/m, resulting in a critical density of the order of $n_c = 3x10^{22}$ m^3. This density accounts for free as well as bound electrons. In the ideal case of 100% assimilation of the injected impurities with homogenous distribution over the pre-disruptive plasma volume of about 830m^3, the amount of gas needed to reach n_c is about 12kPam^3 (Ar), 21kPam^3 (Ne), 57-75kPam^3 (He, D_2). This ideal case is unlikely to be achieved. Present experiments show that the assimilation with MGI is below 20%. SPI can achieve about a factor of 2 higher assimilation of D_2 compared to MGI [55], but the spatial distribution and the potential for further improvement of the assimilation efficiency for SPI (and MGI) remain open questions. For the ideal case, the necessary quantities of He and D_2 exceed the injection limits, whereas argon or neon injection is likely to be compatible with these limits, but because of the high cooling rate of these gases, the CQ time is expected to fall below the eddy current limit. Note that recent experiments performed within the ITPA on low density flat-top RE

pulses, show that the required critical density might be significantly lower [56] [57]. However, understanding the underlying physics and whether this can be confirmed for disruption generated RE remain open issues.

Control of the vertical position of the runaway beam after the generation phase would allow the application of mitigation techniques that act on timescales longer than the CQ time. Such control schemes were successfully applied at ToreSupra [58] and DIII-D [19]. However, even with optimised vertical position of the plasma before the disruption, this control scheme appears unlikely to be feasible at ITER. RE beam control during a disruption from 15 MA using the ITER in-vessel coil would require an initial RE current not lower than 10 MA and a subsequent RE current decay of less than [59].

Runaway electron confinement is sensitive to the existence of MHD activity. It was therefore proposed to inject impurities during the current quench phase to destabilise MHD modes by increasing locally the resistivity. Dedicated experiments at Tore Supra and ASDEX Upgrade showed neither an impact on the current decay nor a correlation of the injection with the observed MHD activity [58]. Magnetic perturbations that are imposed by external coils are able to suppress the formation of a RE beam above a certain amplitude threshold [60] [61]. Modelling for ITER has shown that the perturbation imposed by the in-vessel ELM mitigation coils can create a stochastic layer at the plasma edge only and is therefore not sufficient to ensure RE suppression [62]. Recent measurements at TEXTOR give evidence that intrinsic magnetic broad band fluctuations, arising from the disruptive event itself, may affect the RE beam formation [63]. The implications for RE beam formation in ITER and the controllability of this loss channel needs to be analysed further.

Enhanced loss of RE current is observed when injecting high-Z impurities like argon during the RE plateau phase in DIII-D [19] and ToreSupra [64]. A steady decrease in RE current is also seen at JET with Ar MGI whereas slow gas injection to provoke RE generation usually results in plateaux with constant RE current [65]. Kinetic simulations show that pitch-angle scattering plays a dominant role when high-Z impurities are present in the background plasma in which the RE beam is embedded [66]. The increase in pitch-angle of the scattered runaways leads to a strong increase in synchrotron radiation, which eventually is needed to dissipate the RE energy. This physics picture is supported by the high pitch-angles that are inferred from the estimated energy spectra in experiments [19]. Figure 13 shows simulations with different levels of argon density for a 15MA ITER disruption. The CQ decay has been adjusted to ensure the same level of RE current and RE maximum energy in each case. The energy spectrum is assumed to be dominated by the avalanche with a high average energy. Note, that the spectrum measured in DIII-D has a dominant low energy tail with a high level of isotropy [19]. In the simulation, REs with energies below 100 keV are considered isotropic and don't contribute to the toroidal current. These simulations show that argon densities much below the critical density for avalanche suppression can be sufficient to dissipate the RE energy on a timescale that is given by the vertical movement of the RE beam, which is of the order of 100ms in ITER.

CONCLUSIONS

The design of the ITER plasma facing and structural components is nearly complete. The load specifications that are derived in a conservative approach from the current knowledge on disruption loads are a basis for the design. However, the understanding of disruption physics is an ongoing process and many open issues remain and need to be refined to optimise the operational phase of ITER and to prepare the design for a reliable and efficient disruption mitigation system.

Both, thermal and electromagnetic loads must be carefully monitored throughout the operational phases of ITER, in particular, during early operation on the way to full current and high energy operation. In this phase, the load predictions have to be validated and avoidance and mitigation strategies have to be developed and optimised. For this purpose it will also be inevitable to deliberately perform unmitigated test disruptions at lower current and stored energy.

The potential generation of runaway electrons during disruptions imposes a particular threat to the ITER PFCs. Progress has been made in quantifying the heat load impact, but large uncertainties remain on the energy spectrum and the deposition time, with worst case estimates giving energies that will cause considerable damage to PFCs and even the underlying cooling structure.

The disruption mitigation system is in the design process aiming at finalising the design in 2017. This system will be essential from the start of the first ITER operation campaign, especially because of the implications from all-metal PFCs (increased heat loads and potential melting as well as an increased probability for high electromagnetic loads) and the need to avoid runaway generation. Experiments have shown reliable mitigation of electromagnetic loads using MGI, however, uncertainties remain with respect to the mitigation of thermal loads. Mitigation of runaways appears to be feasible due to a focused effort on this topic in dedicated experiments and modelling. However, these schemes now have to be developed further, to prove they are applicable in ITER. Especially, the sufficiently fast runaway energy dissipation at modest high-Z impurity levels is very promising. Also, if the significantly lower requirements on electron densities for runaway suppression - as observed in flat-top experiments - can be confirmed during disruptions, prevention of runaway formation by raising the electron density can be again considered as a potential mitigation scheme. In view of the very demanding requirements and the remaining uncertainties for disruption/RE mitigation, it is highly desirable to have a most flexible DMS that includes both techniques: shattered pellets and massive gas injection. This system will be essential to ensure successful operation of ITER.

ACKNOWLEGEMENTS

This paper explores new directions for management of disruptions that are not yet introduced into the ITER technical baseline. These results don't commit the nuclear operator. The views and opinions expressed in this paper do not necessarily reflect those of the ITER Organization or the European Commission. This work was part-funded by the RCUK Energy Programme [grant number EP/I501045] and by the European Union's Horizon 2020 research and innovation programme.

REFERENCES

[1]. R. Mitteau et al., Physica Scripta, vol. **T145**, p. 014081, 2011.

[2] . R.A. Pitts et al., Journal of Nuclear Materials, vol. **438**, p. S48, 2013.

[3]. M. Firdaouss et al., Journal of Nuclear Materials, vol. **438**, p. S536, 2013.

[4]. A.R. Raffrey and G. Federici, Journal of Nuclear Materials, vol. **244**, p. 85, 1997.

[5]. A. Loarte et al., in Proc. 20th Int. Conf. on Fusion Energy http://www-naweb.iaea.org/napc/physics/fec/fec2004/datasets/index.html, Vilamoura, Portugal, 2004.

[6]. B. Bazylev et al., Fusion Engineering and Design, vol. **83**, p. 1077, 2008.

[7]. E.M. Hollmann et al., Nuclear Fusion, vol. **45**, p. 1046, 2005.

[8]. D.G. Whyte et al., Journal of Nuclear Materials, Vols. **313-316**, p. 1239, 2003.

[9]. G. Arnoux et al., Journal of Nuclear Materials, vol. **415**, p. S817, 2011.

[10]. M. Lehnen et al., Journal of Nuclear Materials, vol. **438**, p. S102, 2013.

[11]. P.C. de Vries et al., Plasma Physics and Controlled Fusion, vol. **54**, p. 124032, 2012.

[12]. M. Lehnen et al., Nuclear Fusion, vol. **53**, p. 093007, 2013.

[13]. G. Pautasso et al., in 30th EPS Conference on Contr. Fusion and Plasma Phys., ECA Vol. 27A, P-1.135, St. Petersburg, Russia, 2003.

[14]. A.J. Thornton et al., Plasma Phys. Control. Fusion, vol. **54**, p. 125007, 2012.

[15]. R. Granetz et al., Nuclear Fusion, vol. **46**, p. 1001, 2006.

[16]. R.R. Khayrutdinov and V.E. Lukash, J. Comput. Phys., vol. **109**, p. 193, 1993.

[17]. A. Loarte et al., Nuclear Fusion, vol. **51**, p. 073004, 2011.

[18]. J.R. Martin-Solís, Nuclear Fusion, p. submitted, 2014.

[19]. E.M. Hollmann et al., Nuclear Fusion, vol. **53**, p. 083004, 2013.

[20]. K.H. Finken et al., Nuclear Fusion, vol. **30**, p. 859, 1990.

[21]. M. Lehnen et al., Journal of Nuclear Materials, vol. **390**, p. 740, 2009.

[22]. C. Reux et al., in this conference.

[23]. H. Tamai et al., Nuclear Fusion, vol. **42**, p. 290, 2002.

[24]. F. Saint-Laurent, private communication.

[25]. M. Sugihara et al., Nuclear Fusion, vol. **47**, p. 337, 2007.

[26]. S.N. Gerasimov et al., Nuclear Fusion, vol. **54**, p. 073009, 2014.

[27]. S.P. Gerhardt, Nuclear Fusion, vol. **53**, p. 023005, 2013.

[28]. H. Strauss et al., Nuclear Fusion, vol. **54**, p. 043017, 2014.

[29]. N.W. Eidietis et al., to be published, 2014.

[30]. M. Sugihara et al., in Proc. 20th Int. Conf. on Fusion Energy http://www-naweb.iaea.org/napc/physics/fec/fec2004/datasets/index.html, Vilamoura, Portugal, 2004.

[31]. A.R. Polevoi et al., Nuclear Fusion, vol. **53**, p. 123026, 2013.

[32]. G. Pautasso et al., Plasma Phys. Control. Fusion, vol. **51**, p. 124056, 2009.

[33]. C. Reux et al., Nuclear Fusion, vol. **50**, p. 095006, 2010.

[34] . S.A. Bozhenkov et al., Nuclear Fusion, vol. **51**, p. 083033, 2011.

[35]. G. Pautasso et al., Nuclear Fusion, vol. **36**, p. 1291, 1996.

[36]. R. Yoshino et al., Plasma Physics and Controlled Fusion, vol. **39**, p. 313, 1997.
[37]. P.L. Taylor et al., Physics of Plasmas, vol. **6**, p. 1872, 1999.
[38]. V.M. Timokhin et al., Plasma Physics Report, vol. **27**, p. 181, 2001.
[39]. L. Baylor et al., in Proc. 23rd Int. Conf. on Fusion Energy, http://www-naweb.iaea.org/napc/physics/FEC/FEC2010/papers/itr_p1-27.pdf, Daejeon, Korea, 2010.
[40]. N. Commaux et al., Nuclear Fusion, vol. **50**, p. 112001, 2010.
[41]. M. Sugihara et al., in Proceedings of 24th IAEA FEC, ITR/P1-14, San Diego, USA, 2012.
[42]. S.A. Bozhenkov et al., Plasma Physics and Controlled Fusion, vol. **50**, p. 105007, 2008.
[43]. A.J. Thornton et al., Nuclear Fusion, p. 063018, 2012.
[44]. G. Pautasso et al., in Proceedings of the 40th EPS Conference on Plasma Physics, Helsinki, Finland, 2013.
[45]. S. Putvinski et al., in Proc. 23rd Int. Conf. on Fusion Energy, http://www-naweb.iaea.org/napc/physics/FEC/FEC2010/papers/itr_1-6.pdf , Daejeon, Korea, 2010.
[46]. V.A. Izzo, Physics of Plasmas, vol. **20**, p. 056107, 2013.
[47]. R.A. Pitts et al., in this conference, 2014.
[48]. R. Granetz et al., in Proceedings of 24th IAEA FEC, EXP/P8-09, San Diego, USA, 2012.
[49]. I. Landman, "3D Modelling of multiple Massive Gas Injection and First Wall Heating during the Disruption Mitigation Thermal Quench in ITER," in this conference, 2014.
[50]. N. Commaux, in 55th Annual Meeting of the APS Division of Plasma Physics, Volume 58, Number 16 , Denver, CO, USA, 2013.
[51]. G.M. Olynyk et al., Nuclear Fusion, vol. **53**, p. 092001, 2013.
[52]. D.A. Humphreys and A.G. Kellman, Physics of Plasmas, vol. **6**, p. 2742, 1999.
[53]. E.M. Hollmann et al., Plasma Physics, vol. **20**, p. 062501, 2013.
[54]. M. Lehnen et al., Nuclear Fusion, vol. **51**, p. 123010, 2011.
[55]. N. Commaux, Nuclear Fusion, vol. **51**, p. 103001, 2011.
[56]. R. Granetz et al., in 55th Annual Meeting of the APS Division of Plasma Physics, Volume 58, Number 16 , Denver, CO, USA, 2013.
[57]. C. Paz-Soldan et al., Physics of Plasmas, vol. **21**, p. 022514, 2014.
[58]. F. Saint-Laurent et al., Fusion Science and Technology, vol. **64**, p. 711, 2013.
[59]. A. Kavin et al., "Study of ITER plasma position control during disruptions with formation of runaway electrons," ITER report No D3RC46, 2012.
[60]. R. Yoshino and S. Tokuda, Nuclear Fusion, vol. **40**, p. 1293, 2000.
[61]. M. Lehnen et al., Physical Review Letters, vol. **100**, p. 255003, 2008.
[62]. P.B. Aleynikov et al., "Simulations of Runaway Electrons in ITER," in Proceedings of the 37th EPS Conference on Plasma Physics, P1.1004., Dublin, Ireland, 2010.
[63]. L. Zeng, Physical Review Letters, vol. **110**, p. 235003, 2013.
[64]. F. Saint-Laurent, "23rd IAEA Fusion Energy Conference," in http://www-pub.iaea.org/mtcd/meetings/PDFplus/2010/cn180/cn180_papers/exs_p2-16.pdf, 2010.
[65]. V. Riccardo et al., Plasma Physics and Controlled Fusion, vol. **52**, p. 124018, 2010.

[66]. K. Aleynikova, “Interaction of runaway electrons with high-Z impurities,” in 40th European Physical Society Conference on Plasma Physics, Espoo, Finland, 2013.
[67]. E.M. Hollmann et al., Nuclear Fusion, vol. **48**, p. 115007, 2008.
[68]. G. Pautasso et al., Nuclear Fusion, vol. **47**, p. 900, 2007. Figure 7

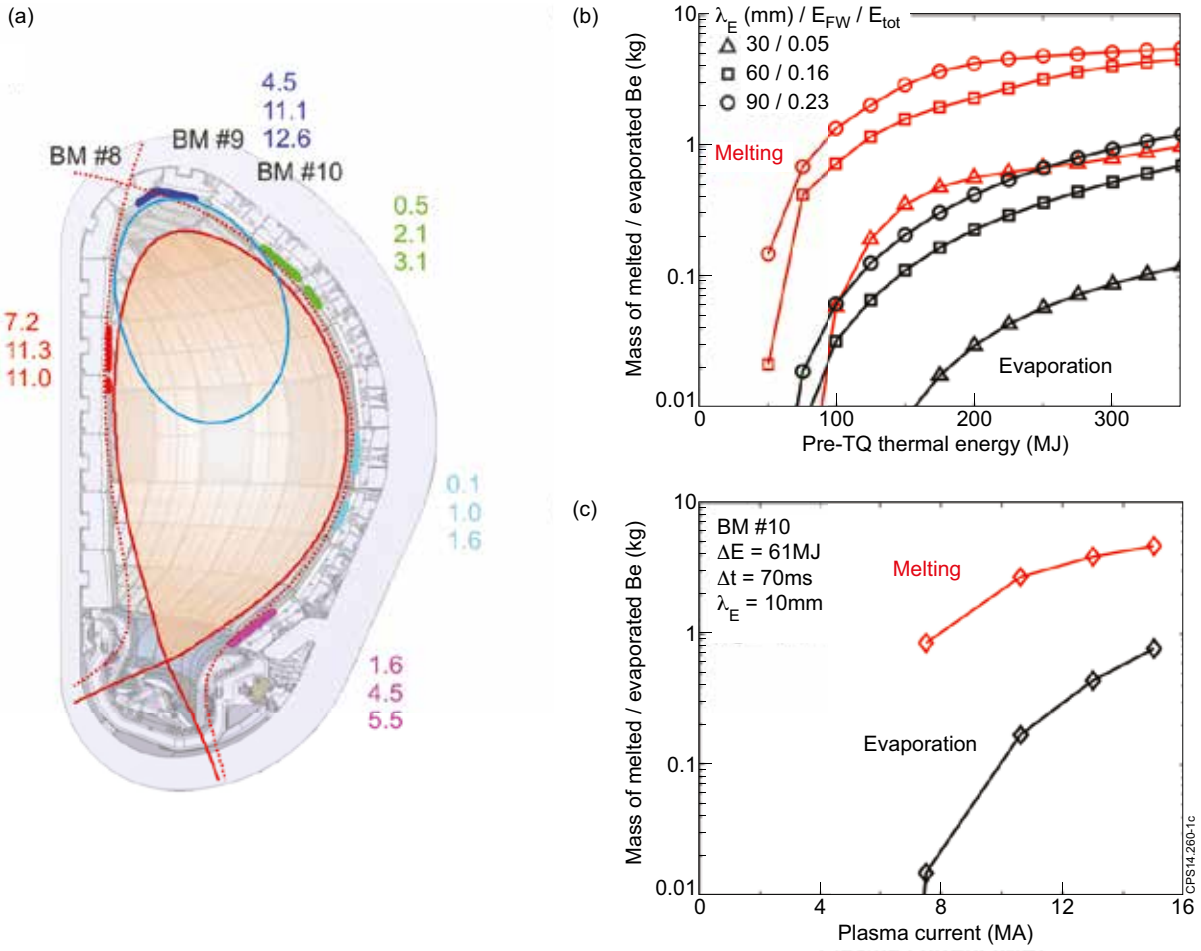

Figure 1: Thermal loads on the first wall (FW) during thermal quench (MD) and current quench (VDE). A) Plasma configuration for the thermal quench loads during the MD (red) and the current quench loads during an upward VDE (blue). The coloured dots indicate the wetted areas for the MD. The current quench loads are mainly on blanket modules 8 to 10. The numbers give the maximum energy impact in MJ/m^2 at 350 MJ stored energy for each of the wetted regions and for λ_E = 30, 60, 90mm. B) mass of melted and evaporated Be during the MD as function of footprint broadening and thermal energy. C) mass of melted and evaporated Be during the VDE current quench for different plasma currents.

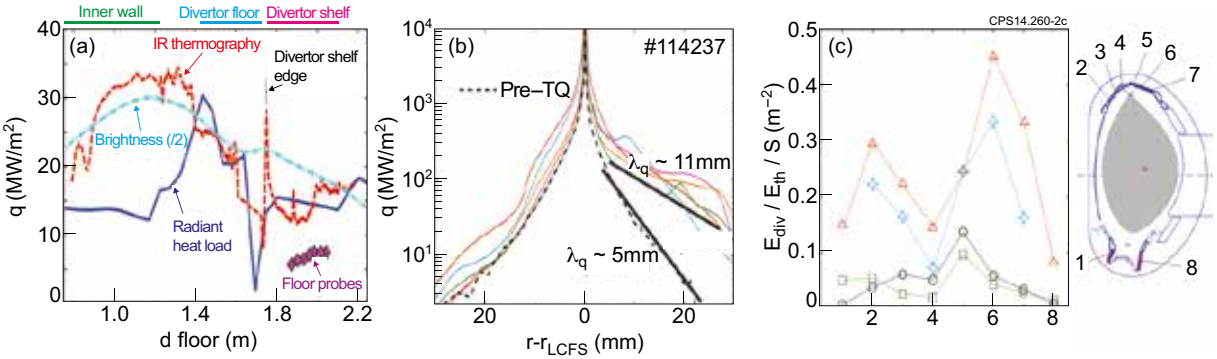

Figure 2:Heat flux distribution during the thermal quench: a) DIII-D perpendicular heat flux to the first wall and lower divertor [53], b) TEXTOR radial profile of parallel heat flux on a spherical test limiter, c) ASDEX-Upgrade first wall and divertor distribution of energy during four density limit disruptions with upper x-point configuration [13].

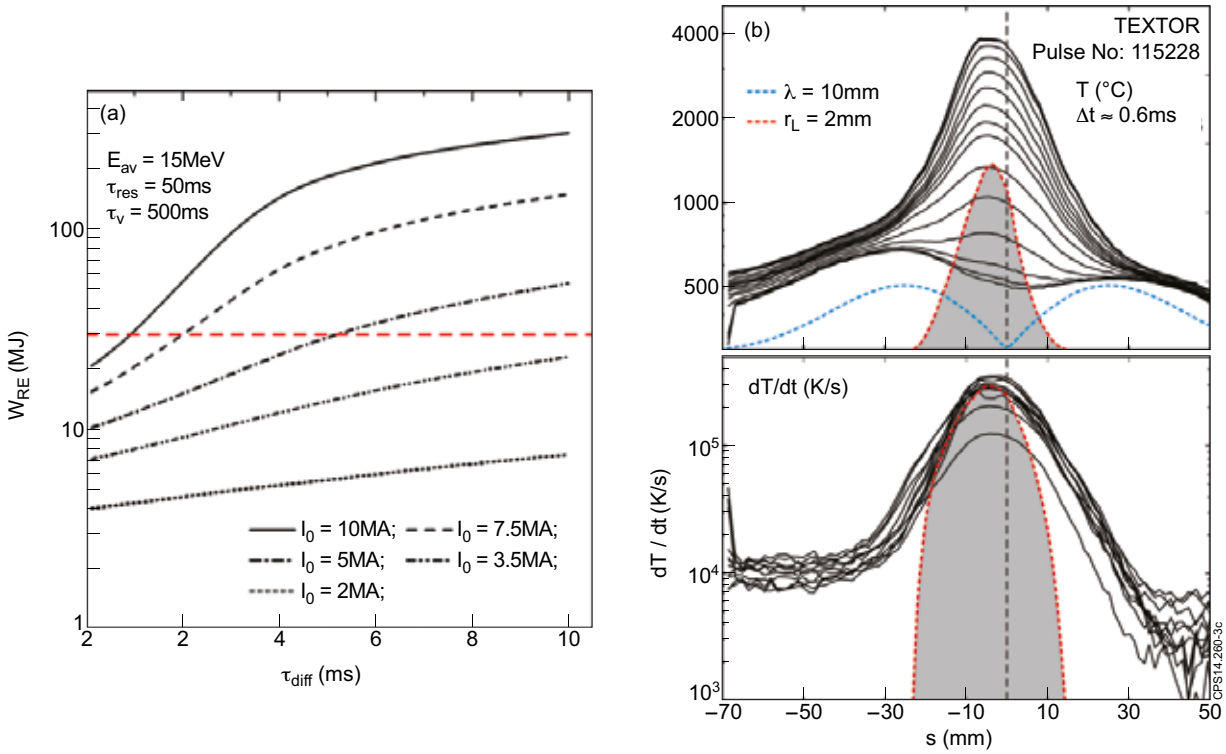

Figure 3: a) Runaway energy increase caused by magnetic energy conversion [18]; b) Runaway electron impact on a spherical test limiter in TEXTOR. The dashed red line indicates surface deposition for a Larmor radius of 2mm.

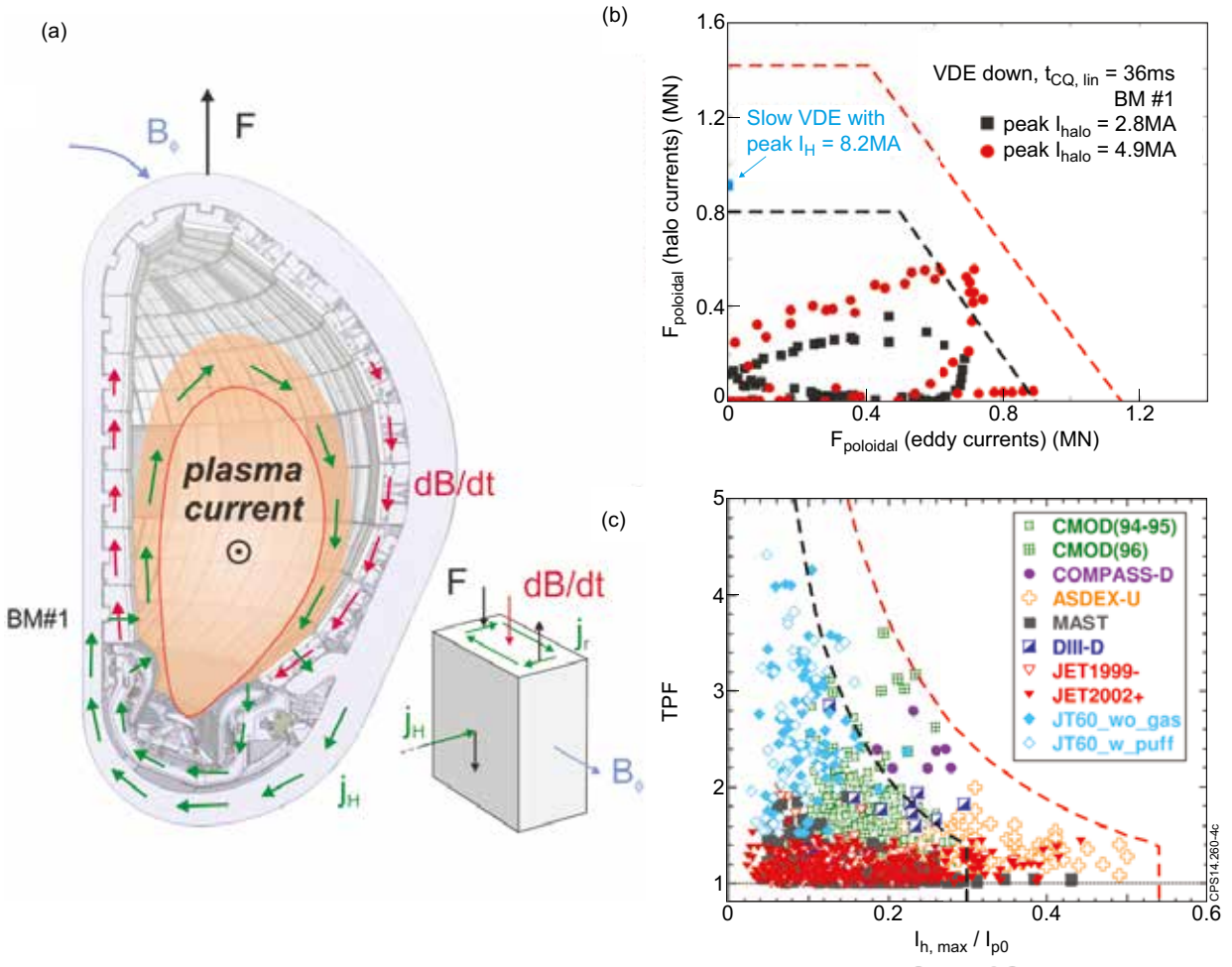

Figure 4: Limits on electro-magnetic loads on the blanket modules and vacuum vessel of ITER. B) Forces from halo and eddy currents on BM 1 during cat II (black dots) and III (red dots) events with 15MA of plasma current. C) Experimentally observed toroidal peaking and halo current fractions [30]. Red dashed lines indicated load limits for category III events, black dashed lines are those for category II events.

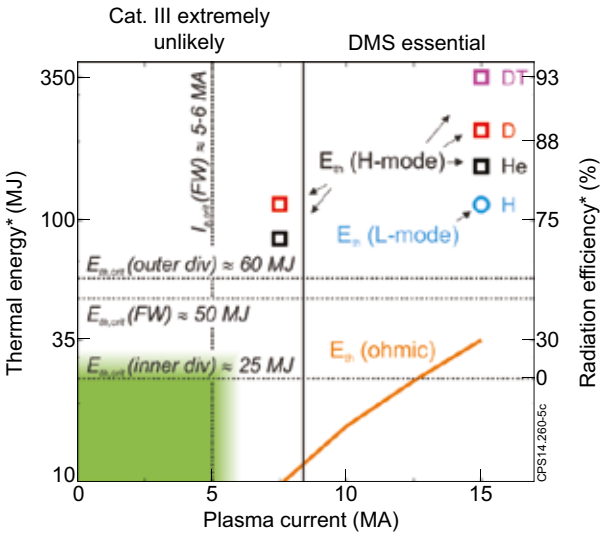

Figure 5: Electro-magnetic and thermal load limits indicating the operational space that requires disruption mitigation.

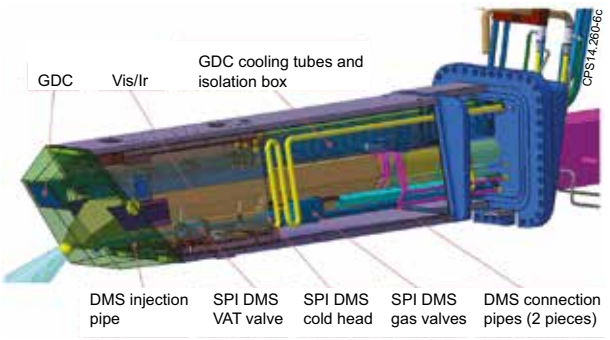

Figure 6: Conceptual design of the integration of a shattered pellet injector in one of the upper port plugs in ITER.

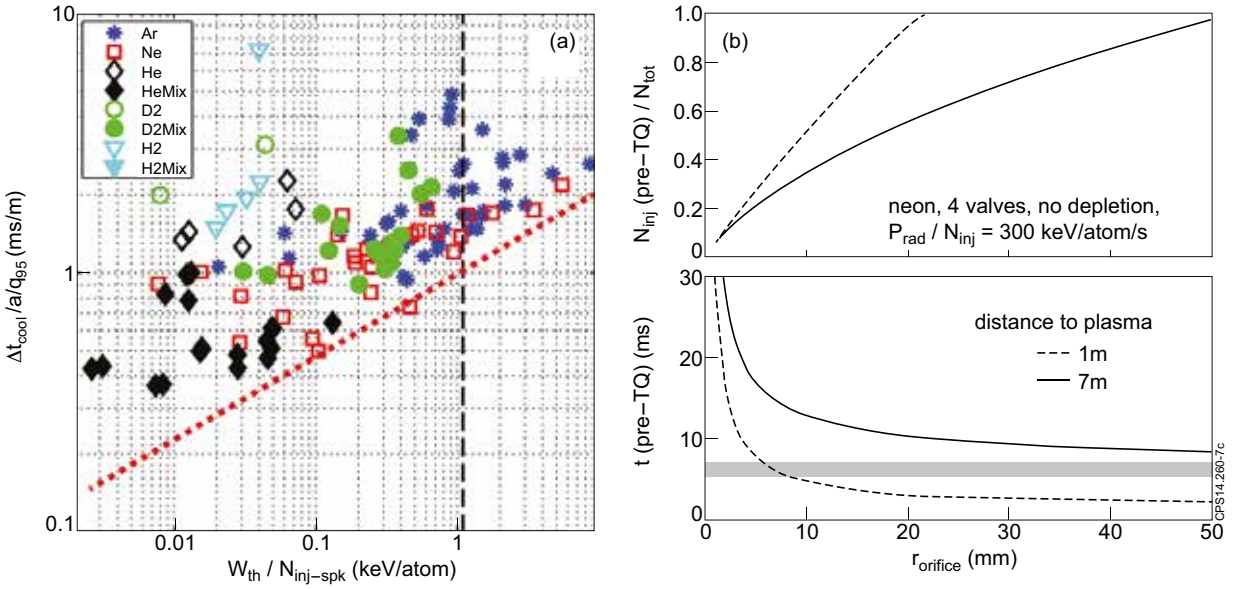

Figure 7: Injection time of a Disruption Mitigation System based on MGI: a) Normalised cooling duration as a function of thermal energy normalised to the number of injected particles (ITPA database, reproduced from [29]); the vertical dashed line indicates the ITER target value for maximum energy. b) Injection efficiency and duration as a function of the diameter of the valve orifice (calculations based on the model described in [34]).

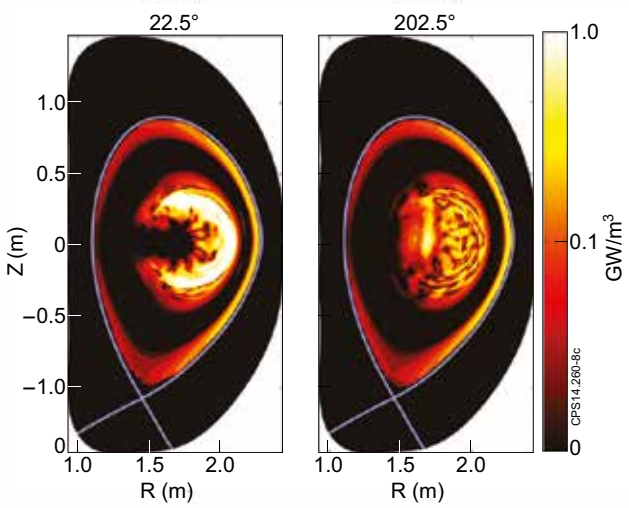

Figure 8: NIMROD simulations for DIII-D MGI with toroidally uniform injection of neon at the low field side: radiation distribution at two toroidal positions, 180° apart, at the time of the thermal quench [46].

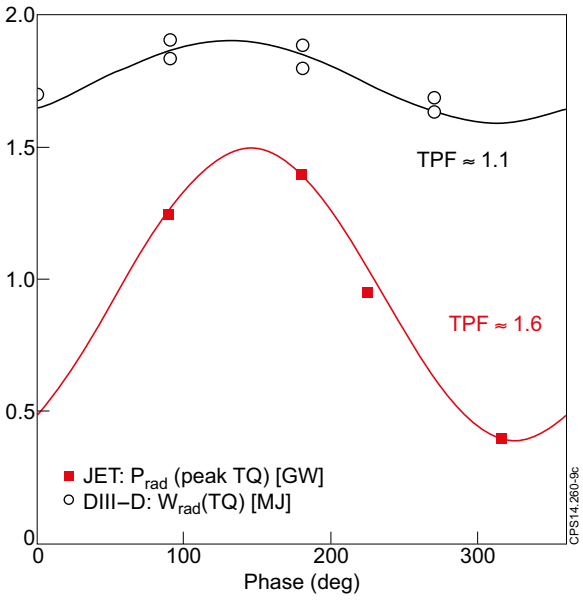

Figure 9: Toroidal radiation distribution in DIII-D [50] and JET with externally applied n=1 field.

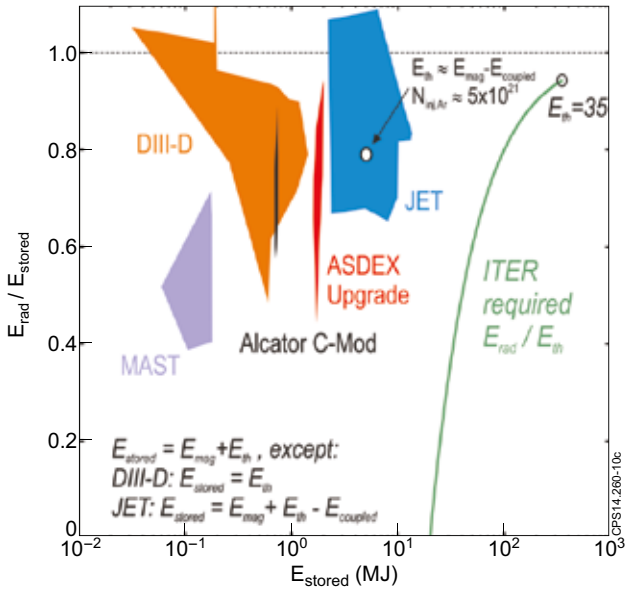

Figure 10: Radiation efficiency during MGI using high-Z noble gases (Ne, Ar) and mixtures of these with D_2 and He. The colored areas indicate the data envelope taken from these publications: [14, 67, 15, 68, 12]. The white JET data point indicates the maximum achievable E_{rad}/E_{stored} for high thermal energy fraction.

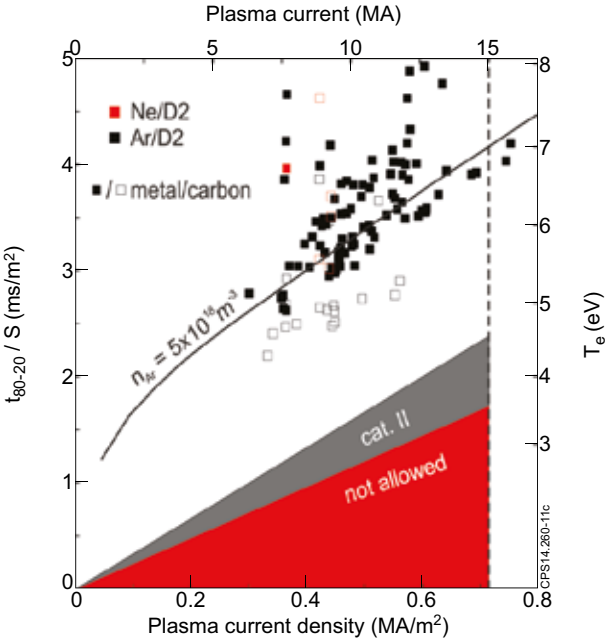

Figure 11: Normalised linear current decay time (S = plasma cross-section area) in JET during injection of Ne and Ar mixed with 90% D_2. The black line represents the CQ time and the electron temperature (right y-axis) as calculated from the power balance [12] for an argon density of 5x1018 m-3 and inductivity L = 3.7μH. Red and gray area indicates the ITER limits on eddy current driven forces for the worst case (S = 21m²).

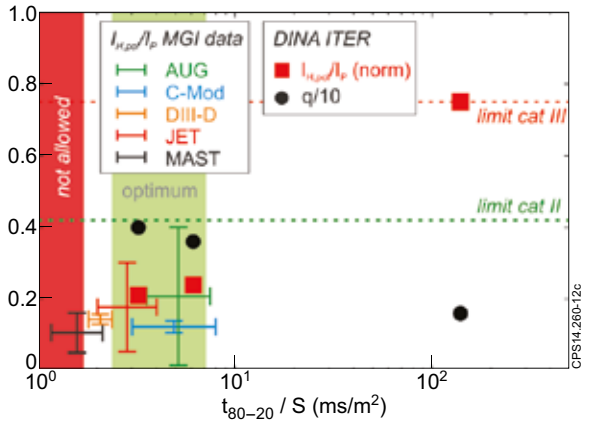

Figure 12: Fraction of poloidal halo current in ITER (red boxes) and safety factor at maximum halo current (black dots) as calculated from DINA. The maximum halo current has been scaled to fit the load limit. Halo current fractions during MGI have been measured in various devices: [68, 15, 53, 54, 14].

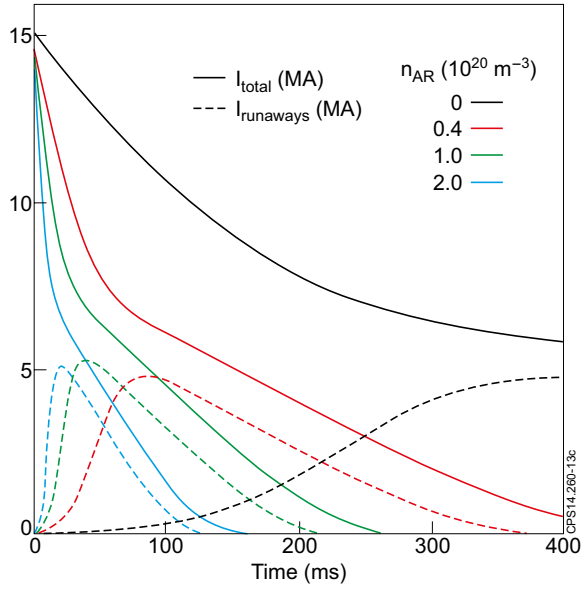

Figure 13: Kinetic simulation of runaway mitigation by collisions with Argon.